

A Computational Study of Spin Hall Effect Device Based on 2D Materials

Tong Wu, and Jing Guo
Corresponding Author: Jing Guo

Email: guoj@ufl.edu

Department of Electrical and Computer Engineering, University of Florida, Gainesville, FL,
32611-6130, USA

ABSTRACT

Efficient spin-charge conversion is indispensable in the spintronic computing and memory technologies for achieving low power. Spin Hall and quantum spin Hall effects have been demonstrated in certain atomically thin two-dimensional (2D) materials. In this work, we develop a multiscale simulation method from atomistic quantum transport simulation to the circuit model for the spin Hall effect (SHE) device based on 2D materials. Numerical implementation to speed up atomistic transport simulations with the non-equilibrium Green's function formalism is described for the crossbar SHE device. The multiscale method can treat atomistic scale features and compute spintronic device performance metrics of the modeled device. As an example, the effect of edge roughness on the SHE devices based on monolayer 2D materials is investigated. The results illustrate that aggressively scaled monolayer SHE devices can efficiently transduce charge to spin in the presence of edge roughness.

I. INTRODUCTION

With the scaling limits of conventional complementary metal-oxide-semiconductor (CMOS) device insight, spintronics has been proposed as an emerging technology for low power computing [1][2]. Efficient spin-charge conversion plays a critically important role in spintronic technologies. For example, in a recently proposed spintronic computing platform [3], devices based on topological spin Hall effect (SHE) and magnetoelectric switching have been demonstrated as the essential components for achieving efficient charge-spin transduction and low-power computing. The SHE devices, which are based on spin-orbit coupling (SOC) of the device channel material, electrically generate or detect spin current in nonmagnetic materials [4]. Significant experimental progress has been achieved on SHE devices based on both metallic and semiconductor material systems [4].

On the other hand, it has been theoretically proposed and experimentally demonstrated that certain two-dimensional (2D) Van der Waals layer materials have SHE or quantum spin Hall effect (QSHE) properties promising for topologically based spin-charge conversion. Due to SOC, which induces topological phases in the band structure, SHE or QSHE appears in 2D nonmagnetic monolayer materials [5][6][7]. The material systems range from the original proposal on SHE in graphene [5] to 2D transition metal dichalcogenide materials (TMDC) [8][9] and Kagome lattice materials [10]. High spin-charge conversion efficiency has been experimentally demonstrated in a TMDC-graphene crossbar device structure at room temperature [8]. Spin and charge transport in 2D topological two-terminal devices have also been theoretically investigated [11].

In this work, we develop a multiscale simulation method and describe its numerical implementation for investigating the SHE device based on the 2D material system. The method treats atomistic scale features and defects in a 2D crossbar device structure and computes the spin-charge conversion efficiency by using a parameterized circuit model. To achieve fast and efficient atomistic device simulations, a numerical implementation, which is based on a carefully designed lattice partition scheme, is proposed to enable the application of a recursive algorithm in the crossbar SHE device structure. The spintronic characteristics of SHE device based on monolayer 2D materials are investigated. In particular, the effect of atomistic edge roughness on spintronic device performance is examined.

II. APPROACH

A multiscale simulation method is developed to simulate spintronic properties for the modeled SHE device structure as shown in Fig. 1. The four contacts of the device are denoted as C1, C2, C3, and C4. The crossbar device structure has been widely used in the Hall effect measurement, as well as the experimental demonstration of room-temperature spin-charge conversion based on 2D materials [8]. In a four-terminal crossbar device, the electrical current flows in the longitudinal direction between the contacts C1 and C3, which results in a spin current in the transverse direction between contacts C2 and C4 due to the SHE and QSHE of the 2D channel material. A multiscale simulation method from atomistic quantum transport simulation to the circuit model of the device, as well as its numerical implementation, are described below.

A. Atomistic simulation by the NEGF formalism

An atomistic tight binding Hamiltonian is used to describe the 2D material channel in the non-equilibrium Green's function (NEGF) quantum transport simulations. For devices in the QSHE transport regime, a 2D monolayer hexagonal lattice structure is used, and the tight binding material parameters are taken to be the same as those in Ref. [5], which has the form of

$$H = \sum_{\langle i,j \rangle \alpha} t c_{i\alpha}^+ c_{j\alpha} + \sum_{\langle\langle i,j \rangle\rangle \alpha\beta} i t_2 v_{ij} S_{\alpha\beta}^z c_{i\alpha}^+ c_{j\beta}, \quad (1)$$

where t is the nearest neighbor hopping parameter, $v_{ij} = -v_{ji} = \pm 1$ depending on the relative orientation of two nearest neighbor bonds, $S_{\alpha\beta}^z$ is the Pauli Z matrix, $t_2 = 0.03t$ is the 2nd nearest neighbor coupling which counts the SOC and responsible for the QSHE. The above tight binding Hamiltonian results in the well-known form of the Kane-Mele Hamiltonian, $H_{so} = \Delta_{so} \psi^+ \sigma_z \tau_z S_z \psi$ [5], where σ_z , τ_z , and S_z are the Pauli Z matrix for sublattice, valley, and spin degrees of freedom respectively, and $\Delta_{so} = 3\sqrt{3}t_2$ is the SOC parameter, which determines the bandgap opened by the SOC effect. Although the experimental demonstration of QSHE in graphene is challenging, the QSHE has been experimentally demonstrated in 2D TMDC materials [9].

In addition, to simulate the 2D QSHE device, SHE device based on monolayer TMDC materials at the 2H crystalline phase, which has only a topologically trivial band structure but nonzero topological phases, is simulated. The Hamiltonian can be expressed as [6],

$$H = \frac{\Delta}{2} \sigma_z + \sum_{\langle i,j \rangle \alpha} t c_{i\alpha}^+ c_{j\alpha} + \lambda \tau \frac{\sigma_z - 1}{2} S_z, \quad (2)$$

where Δ is the sublattice on-site potential difference, and λ is one half of spin splitting determined by SOC. As an example of TMDC material, the parameters for MoS₂ are $\Delta = 1.66$ eV, $t = 1.10$ eV, and $\lambda = 0.075$ eV.

Equations (1) and (2) are the Hamiltonians used in this study for 2D materials with the SHE and QSHE phenomena, respectively. It is noted that several types of tight binding Hamiltonian have been proposed to describe these effects in 2D structures [12], and the multiscale simulation approach is general and not restricted to the specific form of the Hamiltonian.

Once the Hamiltonian is determined, the retarded Green's function is calculated as [13],

$$G^r(E) = [(E + i0^+)I - H_D - \sum_{i=1}^4 \Sigma_i]^{-1}, \quad (3)$$

where H_D is the tight binding Hamiltonian of the crossbar device channel, Σ_i is the contact self-energy of the i -th contact, with the index i summing over contacts C1 to C4 for the device in Fig. 1. Ballistic transport and semi-infinite contacts are assumed for simplicity. The mutual charge transmission between any two contacts, T_{ij} , where $1 \leq i, j \leq 4$, can be expressed as,

$$T_{ij} = \text{trace}(G^r \Gamma_i G^{r+} \Gamma_j), \quad (4)$$

where Γ_i and Γ_j are broadening of the physical contacts i and j , respectively. The spin transmission due to applied charge voltages can be computed as,

$$T_{ij}^{sc} = \text{trace}(\boldsymbol{\sigma} G^r \Gamma_i G^{r+} \Gamma_j), \quad (5)$$

where $\boldsymbol{\sigma}$ are the Pauli matrices. For the spin colinear cases where the spin polarization is along the z-direction, $\boldsymbol{\sigma}$ can be simplified to σ_z , thus T_{ij}^{sc} can be simplified to T_{ij}^{zc} .

Since the tight banding Hamiltonian provides an atomistic description of the device channel, the atomistic scale edge roughness or defects can be treated by removing the corresponding atoms in the 2D material channel. For a specified probability of edge roughness or defect percentage, a sufficiently large number of device samples are stochastically generated and simulated. The physical quantities of interest are obtained by statistically averaging over these devices. Because of the need to simulate a large number of devices, computational efficiency is important.

A straightforward evaluation of the charge and spin transmission, T_{ij} and T_{ij}^{zc} by Eqs. (4) and (5), respectively, requires off-diagonal blocks of the Green's function G^r between the atom blocks i and block j . For the modeled four-terminal device, multiple off-diagonal blocks at different off-diagonal sites are needed for computing all mutual transmissions. A direct inversion of the

Hamiltonian to obtain all these off-diagonal blocks can be computationally inefficient. An efficient numerical implementation, thereby, is developed and described next for the four-terminal device.

B. Numerical implementation

To address the computational efficiency issue of the NEGF simulations, a recursive algorithm, which has previously been applied to two-terminal and three-terminal devices [14], is extended to four-terminal crossbar devices. The recursive algorithm takes advantage of the block tridiagonal structure of the Hamiltonian, and computes the diagonal blocks and certain off-diagonal blocks of the Green's function. The application of the recursive algorithm requires that each lattice block only couples to its neighboring blocks, so that the Hamiltonian matrix has a block tridiagonal structure. A lattice partition method of the four-terminal crossbar device is designed to achieve this goal, as shown in Fig. 2(a). Each box denotes a block of the device channel, which only couples to its neighboring block lattices for implementing the recursive algorithm. In the crossbar region, the size of the blocks becomes progressively larger from left to right. Figure 2(b) shows the topological arrangement of the blocks. In this scheme, the left contact in computation is essentially the physical contact C1, and the right contact for computation is combined physical contacts C2, C3, and C4. For semi-infinite contacts, the self-energy can be computed by using the Sancho-Rubio scheme [15].

A straightforward evaluation of charge and spin transmission coefficients by Eqs. (4) and (5) requires an off-diagonal block of the Green's function G^r between the atom block \underline{i} and block j . For the partition scheme as shown in Fig. 2(a), the Green's function blocks between any two of the contacts C2, C3 and C4 can be evaluated directly, because they belong to the same computational block N , which provides the required matrix elements. Therefore, the mutual transmissions T_{23} , T_{24} and T_{34} between any two of C2, C3 and C4 can be straightforwardly computed. However, the Green's function blocks between contact C1 and any other contacts are not available from the blocks of G^r calculated by the recursive algorithm. This problem can be addressed by noticing the following relation for the lumped sum S_i of the charge transmission coefficients,

$$S_i = \sum_{j \neq i} T_{ij} = \text{trace}(G^r \Gamma_i G^{r+} \sum_{j \neq i} \Gamma_j) = \text{trace}(i(G_i^r - G_i^{r+}) - G^r \Gamma_i G^{r+} \Gamma_i). \quad (6)$$

Evaluation of Eq. (6) only requires the i -th diagonal block of G^r . By using Eq. (6) to compute the lumped sum of the transmission S_i for $i = 2, 3, 4$, and noticing the symmetric relation $T_{ij} = T_{ji}$ for the charge transmission coefficients, the values of T_{12} , T_{13} and T_{14} can be solved as,

$$\begin{bmatrix} T_{12} \\ T_{13} \\ T_{14} \end{bmatrix} = \begin{bmatrix} S_2 \\ S_3 \\ S_4 \end{bmatrix} - \begin{bmatrix} T_{23} + T_{24} \\ T_{23} + T_{34} \\ T_{24} + T_{34} \end{bmatrix}. \quad (7)$$

For calculating the spin transmission coefficient T_{ij}^{zc} , a similar procedure can be applied for the mutual transmissions between any two of the contacts C2, C3, and C4 by using Eq. (5). To compute the mutual spin transmission between the contact C1 and other contacts, the lumped sum of the spin transmission to contact C_i due to charge voltages is expressed as,

$$S_i^{zc} = \sum_{j \neq i} T_{ij}^{zc} = \text{trace}(\sigma_z G^r \Gamma_i G^{r+} \sum_{j \neq i} \Gamma_j) = \text{trace}(i\sigma_z (G_i^r - G_i^{r+}) - \sigma_z G^r \Gamma_i G^{r+} \Gamma_i). \quad (8)$$

In contrast to the charge transmission, which is symmetric to index order, the spin transmission is antisymmetric $T_{ij}^{zc} = -T_{ji}^{zc}$ for the system with time-reversal symmetry. By using this relation together with the lump sum spin transmission $S_i^{zc} = \sum_{j \neq i} T_{ij}^{zc}$ for $i = 2, 3, 4$, the mutual spin transmissions between the contact C1 and other three contacts can be solved as,

$$\begin{bmatrix} -T_{12}^{zc} \\ -T_{13}^{zc} \\ -T_{14}^{zc} \end{bmatrix} = \begin{bmatrix} S_2^{zc} \\ S_3^{zc} \\ S_4^{zc} \end{bmatrix} - \begin{bmatrix} T_{23}^{zc} + T_{24}^{zc} \\ -T_{23}^{zc} + T_{34}^{zc} \\ -T_{24}^{zc} - T_{34}^{zc} \end{bmatrix}. \quad (9)$$

The speedup of the atomistic simulations, which is the most time-consuming part of the overall multiscale task, stems, from the above partition scheme with the application of the recursive algorithm as described in Fig. 2. For a crossbar structure with a horizontal ribbon index of m and a vertical ribbon index of n , the crossbar central part has $m \times n$ atoms. Direct calculation of the Green's function has a computational cost of $\sim O(m^3 \times n^3)$ due to matrix inversion, for a size determined by the number of atoms of $\sim m \times n$. With the recursive algorithm, the computational cost becomes $\sim O((m+n)^3 \times n)$, because only the partitioned subblocks need to be inverted. The speedup is in the order of ~ 100 for m and n in the order of several tens, and it becomes even more significant as the device size increases. This algorithm takes advantage of the carefully designed partition scheme and does not sacrifice the accuracy of simulation.

C. Circuit model

In the multiscale simulation framework, the atomistic quantum transport simulation is used to parameterize a spin circuit model for the crossbar device. Based on the parameterized model, the

spintronic device performance, such as the spin Hall angle, can be computed. For a colinear spintronic device modeling, the charge current and the spin current can be expressed as [16],

$$\begin{bmatrix} \tilde{I}^c(E) \\ \tilde{I}^z(E) \end{bmatrix} = \frac{1}{q} \begin{bmatrix} \tilde{G}^{cc} & \tilde{G}^{cz} \\ \tilde{G}^{zc} & \tilde{G}^{zz} \end{bmatrix} \begin{bmatrix} f^c(E) \\ f^z(E) \end{bmatrix} = \frac{1}{q} \left\{ \begin{bmatrix} \tilde{G}^{cc} \\ \tilde{G}^{zc} \end{bmatrix} f^c(E) + \begin{bmatrix} \tilde{G}^{cz} \\ \tilde{G}^{zz} \end{bmatrix} f^z(E) \right\}, \quad (10)$$

where $\tilde{I}^c(E)$ and $\tilde{I}^z(E)$ are the charge and spin current spectrum vectors, q is the elementary electron charge, $f^c(E)$ and $f^z(E)$ are the Fermi-Dirac distribution vectors for charge and spin, respectively, spanned over the contact index space, \tilde{G}^{cc} and \tilde{G}^{zc} are the charge and spin conductance matrices due to charge voltages, and \tilde{G}^{cz} and \tilde{G}^{zz} are the conductance matrices due to applied spin voltages. Fig. 3(a) schematically shows the edge modes of the QSHE crossbar device, and the current and Fermi function vectors for each contact are denoted. The modeled device system satisfies time-reversal symmetry, and the contacts are non-magnetic. As a result, the spin entries of the Fermi function are zero, $f^z(E)=0$, which further simplifies Eq. (10) to the following expression for the charge and spin currents in the linear response regime,

$$\begin{aligned} I_i^c &= \frac{1}{q} \sum_j G_{ij}^{cc} E_{Fj}, \\ I_i^z &= \frac{1}{q} \sum_j G_{ij}^{zc} E_{Fj}, \end{aligned} \quad (11)$$

where I_i^c , and I_i^z are the charge and spin currents at contact C_i , respectively, and E_{Fj} is the Fermi level E_F at contact C_j . The mutual charge (spin) conductance is proportional to the charge (spin) transmission from the NEGF transport simulation described above,

$$\begin{aligned} G_{ij}^{cc} &= \frac{q^2}{h} T_{ij}, \\ G_{ij}^{zc} &= \frac{q^2}{h} T_{ij}^{zc}, \end{aligned} \quad (12)$$

where h is the Planck constant. Fig. 3(b) shows the equivalent linear circuit model, in which the conductance values are denoted for $i < j$. The charge conductance and spin conductance are symmetric and antisymmetric, respectively, when the indices i and j are commuted.

By computing the charge and spin currents of all 4 contacts, the spin Hall angle, which characterizes the spin-charge transduction efficiency as the ratio between the induced transverse spin current to the longitudinal electrical charge current, can be computed as,

$$\theta_{SH} = \left| \frac{I_2^z - I_4^z}{I_1^c - I_3^c} \right|. \quad (13)$$

The multiscale simulation method described above allows the treatment of atomistic scale features and defects in the quantum transport simulations, and subsequently parameterizes the transport properties into a circuit model, from which the spintronic device performance can be assessed. The efficient numerical implementation allows to simulate and average over a large number of random device samples for modeling the effect of random disorders.

III. RESULTS

The carrier transport and spintronic device performance in the crossbar device structure are examined for the monolayer TMDC materials. We first examine the device at the QSHE transport regime described by the Hamiltonian in Eq. (2). In patterning a nanoscale device, the edge roughness is inevitable. The effect of edge roughness on the spin density is examined. Fig. 4 shows the spin density calculated at energy $E = 0$ for four samples with different degrees of edge roughness. Previously, it has been shown that vacancies at 2D topological insulator edges can result in bound states, impact local electronic structure at edges, and deteriorate topologically protected transport [17][18]. The edge roughness is created by removing the atoms in the outmost atomistic edge line with a specified probability. The results show perfect antisymmetric spin densities at two edges of the device with ideal edges. Edge roughness results in significantly different spin density distributions at the rough edges, especially as the roughness percentage increases. In the atomistic sites where edge roughness exists, the spin density drastically reduces. The edge roughness results in a large perturbation to the lattices at the defective sites, and thereby, the local spin density at the defective sites.

Next, we examine the effect of edge roughness on the spin-charge transduction efficiency in the crossbar device. Figure 5 shows the calculated spin Hall angle for two crossbar sizes with various edge roughness. The vertical armchair-edge ribbon is chosen to have an index of $n=3p+2$, where p is an integer, in which quantum confinement alone does not result in a band gap [19]. For the horizontal zigzag-edge nanoribbon, quantum confinement effect alone does not open a bandgap for any index m . The results for two crossbar sizes, with a larger one in Fig. 5(a) and smaller one in Fig. 5(b), are shown here to illustrate the impact of the crossbar device size. Devices with other size parameters have also been simulated, which show the same physical trend. Figure 5(a) shows that with perfect edges, the spin Hall angle approaches the ideal value of 1 when the Fermi level is placed in the bandgap created by SOC. For a further scaled device with a smaller size as shown

in Fig. 5(b), the spin Hall angle for the perfect edges also approaches 1. As the edge roughness percentage increases, these two devices, however, show different sensitivity to edge roughness. For the wider device in Fig. 5(a), the spin Hall angle changes by a smaller amount when the edge roughness percentage increases from 5% to 20% in the low energy range. In contrast, in the narrower ribbon in Fig. 5(b), the spin Hall angle decreases by a larger amount. The reason is that as the edge width decreases, the spatial overlap between two edge modes increases, which weakens the topologically protected transport properties. The spin Hall angle in the narrower device, however, is still >0.2 in the presence of 20% edge roughness. In addition, the spin Hall angle shows a dip near the energy of $E=0$, which is due to the nanostructured size effect of the crossbar structure, and the depth of the dip decreases as the crossbar size increases, as shown by shallower dip in Fig. 5(a) compared to Fig. 5(b). The results indicate that although the topologically protected edge modes in principle can achieve high values of the spin Hall angle for the channel material with QSHE, edge quality and device size play an important role in the spin-charge transduction efficiency when the device is scaled down.

At last, we examine the SHE devices based on TMDC materials at the 2H phases with the Hamiltonian in Eq. (2). Compared to the QSHE device examined above, the channel materials are topologically trivial, but the berry phases are nonzero. These properties of the monolayer MoS₂ have been experimentally utilized in a crossbar structure for room-temperature spin-charge transduction [8]. Fig. 6(a) shows the energy-resolved charge and spin conductance in the valence band for the crossbar device with ideal edges. The charge conductance is calculated as $G^c = \frac{\partial I_1^c}{\partial V_D}$ and the spin conductance is calculated as $G^z = \frac{\partial I_2^z}{\partial V_D}$, for the device structure as shown in Fig. 1. Away from the valence band edge, the charge conductance increases due to a larger number of modes for charge transport. In comparison, the spin conductance is considerably smaller and does not increase as a function of energy difference to the valence band edge. The spin Hall angle, therefore, is smaller than that of the QSHE device investigated in Fig. 5, which represents the upper limit when the bands are topologically inverted. To examine the effect of edge roughness, Fig. 6(b) plots the spin Hall angle with different percentages of edge roughness. For the modeled nanoscale MoS₂ crossbar device structure, the simulation results show that the operation near the valence band edge is more desirable for a larger spin Hall angle. In addition, the peak value of the spin Hall angle reaches a value of >0.2 for ideal edges and a spin Hall angle of 0.15 is still obtained

in the presence of 20% edge roughness in an energy range wider than room-temperature thermal energy, which indicates that the 2D TMDC crossbar device is promising for efficient room-temperature spin-charge conversion even when the device is scaled down to ~ 10 nm-scale device channel size.

IV. CONCLUSIONS

A multiscale simulation framework is developed to simulate the SHE crossbar devices based on 2D materials. Numerical implementation to speed up the NEGF atomistic simulation of the crossbar spintronic device is discussed. This method is applied to simulate the spintronic and quantum transport properties of the four-terminal SHE and QSHE devices based on monolayer 2D materials. The results show that edge roughness plays an important role in the device properties and charge-spin transduction efficiency. The impact of the edge roughness is strongly dependent on the width of the device channel. Even in the presence of edge roughness, the aggressively scaled monolayer SHE devices based on 2D materials still show promising performance for spin-charge conversion.

Acknowledgment

This work was supported by NSF Awards #1809770 and #1904580.

Data Availability Statement

The data that support the findings of this study are available from the corresponding author upon reasonable request.

References

- [1] S. A. Wolf, D. D. Awschalom, R. A. Buhrman, J. M. Daughton, S. von Molnár, M. L. Roukes, A. Y. Chtchelkanova, and D. M. Treger, “Spintronics: A Spin-Based Electronics Vision for the Future,” *Science*, vol. 294, no. 5546, pp. 1488–1495, Nov. 2001.
- [2] A. Fert, “Nobel Lecture: Origin, development, and future of spintronics,” *Rev. Mod. Phys.*, vol. 80, no. 4, pp. 1517–1530, Dec. 2008.
- [3] S. Manipatruni, D. E. Nikonov, C.-C. Lin, T. A. Gosavi, H. Liu, B. Prasad, Y.-L. Huang, E. Bonturim, R. Ramesh, and I. A. Young, “Scalable energy-efficient magnetoelectric spin-orbit logic,” *Nature*, vol. 565, no. 7737, pp. 35–42, Jan. 2019.
- [4] T. Jungwirth, J. Wunderlich, and K. Olejník, “Spin Hall effect devices,” *Nature Materials*, vol. 11, no. 5, pp. 382–390, May 2012.
- [5] C. L. Kane and E. J. Mele, “Quantum Spin Hall Effect in Graphene,” *Phys. Rev. Lett.*, vol. 95, no. 22, p. 226801, Nov. 2005.
- [6] D. Xiao, G.-B. Liu, W. Feng, X. Xu, and W. Yao, “Coupled Spin and Valley Physics in Monolayers of MoS₂ and Other Group-VI Dichalcogenides,” *Phys. Rev. Lett.*, vol. 108, no. 19, p. 196802, May 2012.
- [7] X. Qian, J. Liu, L. Fu, and J. Li, “Quantum spin Hall effect in two-dimensional transition metal dichalcogenides,” *Science*, vol. 346, no. 6215, pp. 1344–1347, Dec. 2014.
- [8] C. K. Safeer, J. Ingla-Aynés, F. Herling, J. H. Garcia, M. Vila, N. Ontoso, M. R. Calvo, S. Roche, L. E. Hueso, and F. Casanova, “Room-Temperature Spin Hall Effect in Graphene/MoS₂ van der Waals Heterostructures,” *Nano Lett.*, vol. 19, no. 2, pp. 1074–1082, Feb. 2019.
- [9] S. Wu, V. Fatemi, Q. Gibson, K. Watanabe, T. Taniguchi, R. J. Cava, and P. Jarillo-Herrero, “Observation of the Quantum Spin Hall Effect Up to 100 Kelvin in a Monolayer Crystal,” *Science*, vol. 359, no. 6371, pp. 76–79, 2018.
- [10] L. Ye, M. Kang, J. Liu, F. von Cube, C. R. Wicker, T. Suzuki, C. Jozwiak, A. Bostwick, E. Rotenberg, D. C. Bell, L. Fu, R. Comin, and J. G. Checkelsky, “Massive Dirac fermions in a ferromagnetic kagome metal,” *Nature*, vol. 555, no. 7698, pp. 638–642, Mar. 2018.
- [11] X. Dang, J. D. Burton, A. Kalitsov, J. P. Velev, and E. Y. Tsybal, “Complex band structure of topologically protected edge states,” *Phys. Rev. B*, vol. 90, no. 15, p. 155307, Oct. 2014.
- [12] L. Fu and C. L. Kane, “Topological insulators with inversion symmetry,” *Phys. Rev. B*, vol. 76, no. 4, p. 045302, Jul. 2007.
- [13] S. Datta, *Quantum Transport: Atom to Transistor*. Cambridge University Press, 2005.
- [14] N. Papior, N. Lorente, T. Frederiksen, A. García, and M. Brandbyge, “Improvements on non-equilibrium and transport Green function techniques: The next-generation transiesta,” *Computer Physics Communications*, vol. 212, pp. 8–24, Mar. 2017.
- [15] M. Sancho, J. Sancho, J. M. L. Sancho, and J. Rubio, “Highly Convergent Schemes for the Calculation of Bulk and Surface Green Functions,” *Journal of Physics F*, vol. 15, p. 851.
- [16] K. Y. Camsari, S. Ganguly, D. Datta, and S. Datta, “Non-Equilibrium Green’s Function Based Circuit Models for Coherent Spin Devices,” *IEEE Trans. Nanotechnology*, vol. 18, pp. 858–865, 2019.
- [17] W.-Y. Shan, J. Lu, H.-Z. Lu, and S.-Q. Shen, “Vacancy-induced bound states in topological insulators,” *Phys. Rev. B*, vol. 84, no. 3, p. 035307, Jul. 2011.

- [18] X. Ni, H. Huang, and F. Liu, “Robustness of topological insulating phase against vacancy, vacancy cluster, and grain boundary bulk defects,” *Phys. Rev. B*, vol. 101, no. 12, p. 125114, Mar. 2020.
- [19] K. Nakada, M. Fujita, G. Dresselhaus, and M. S. Dresselhaus, “Edge state in graphene ribbons: Nanometer size effect and edge shape dependence,” *Phys. Rev. B*, vol. 54, no. 24, pp. 17954–17961, Dec. 1996.

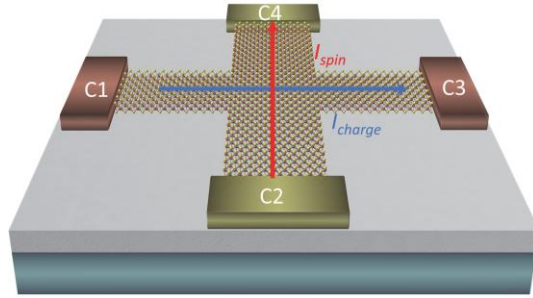


FIG. 1. Schematic structure of the modeled crossbar device based on the quantum spin Hall or spin Hall effect of the 2D layered material channel. A voltage is applied between the contact C1 and contact C3 with $V_1 = V_D/2$ and $V_3 = -V_D/2$, which induces a transverse spin current between contacts C2 and C4. The transverse contacts C2 and C4 are biased at $V_2 = V_4 = 0$, which results in only spin current without charge current between C2 and C4.

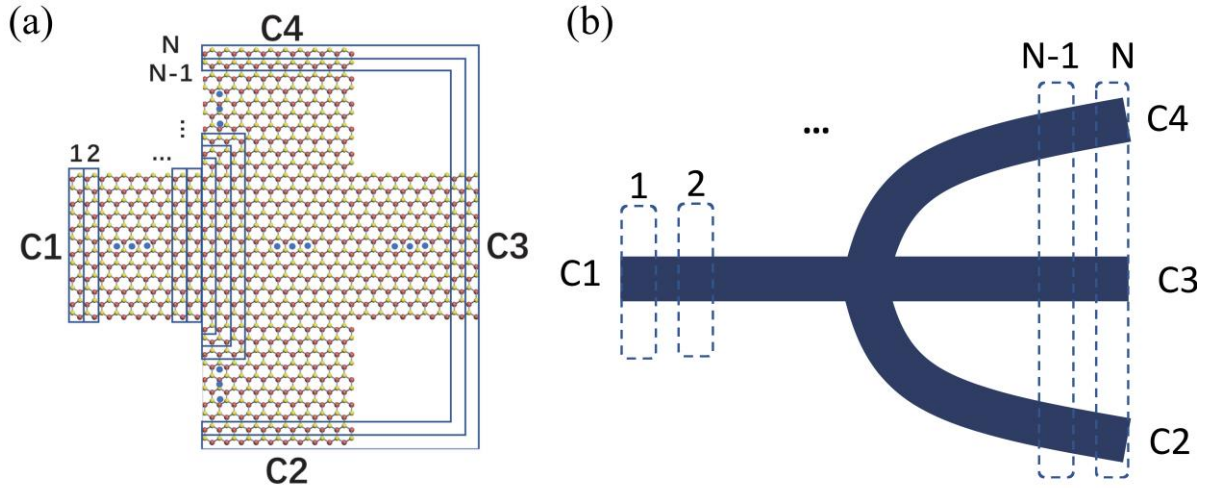


FIG. 2. (a) A lattice partition scheme for numerical implementation of the recursive algorithm in quantum transport simulations of the four-terminal crossbar device. The contacts of the crossbar device structures are assumed to be semi-infinite ribbons. The subblocks are indexed from 1 to N , in which each subblock couples only to its neighboring subblocks. (b) Schematic structure of the crossbar device that illustrates the topological structure for implementing the recursive algorithm. The first subblock is connected to the physical contact $C1$, and the last subblock is connected to the physical contacts $C2$, $C3$, and $C4$.

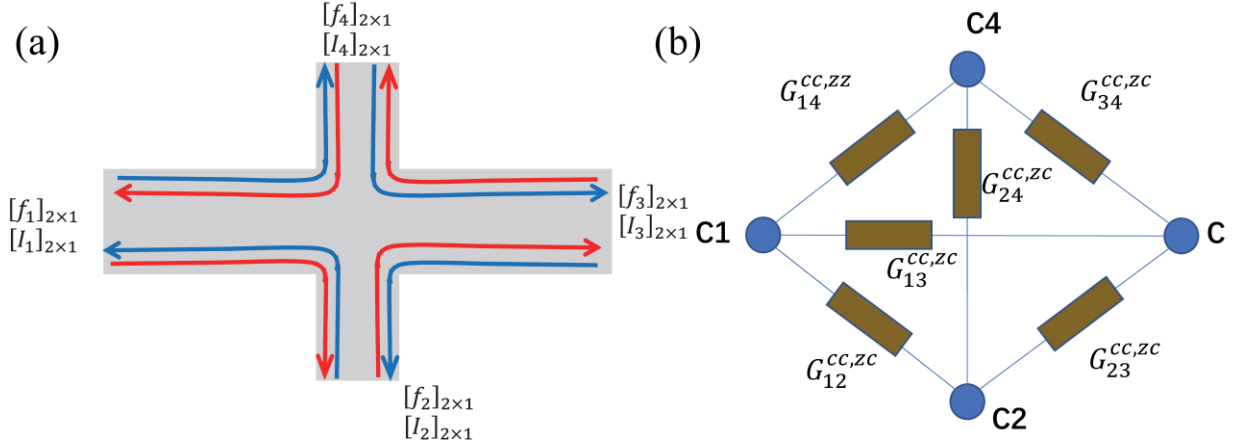


FIG. 3. (a) Schematic plot of the edge modes in a QSHE crossbar device. For colinear simulations, both the Fermi Dirac distribution, f_i , and the current, I_i , at contact i have two components, one for charge and the other for spin. The blue and red arrows represent these spins, as well as the directions of the edge mode currents. (b) The equivalent circuit model for the crossbar spin Hall effect device. Only the conductance elements, G_{ij}^{cc} and G_{ij}^{zc} , with $i < j$ are shown. The charge conductance satisfies $G_{ij}^{cc} = G_{ji}^{cc}$ and the spin conductance satisfies $G_{ij}^{zc} = -G_{ji}^{zc}$ in a system with time-reversal symmetry. The modeled device structure is shown in Fig. 1.

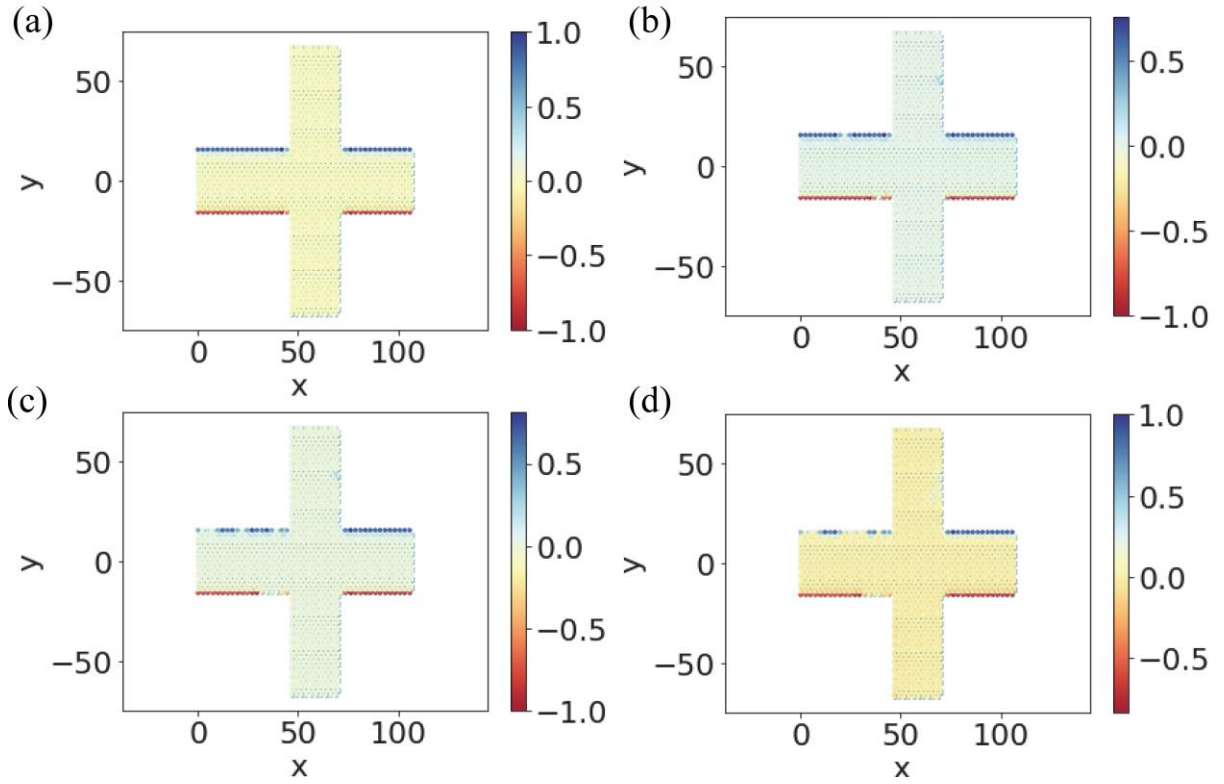


FIG. 4. Simulated normalized spin density in the crossbar device with monolayer 2D material channel for (a) perfect edges, and defective edges with (b) 5%, (c) 10%, and (d) 20% edge roughness. The horizontal part of the crossbar structure has zigzag edges, and the vertical part of the crossbar structure has armchair edges. The x and y positions have a unit of Angstrom, \AA . The modeled device structure is shown in Fig. 1.

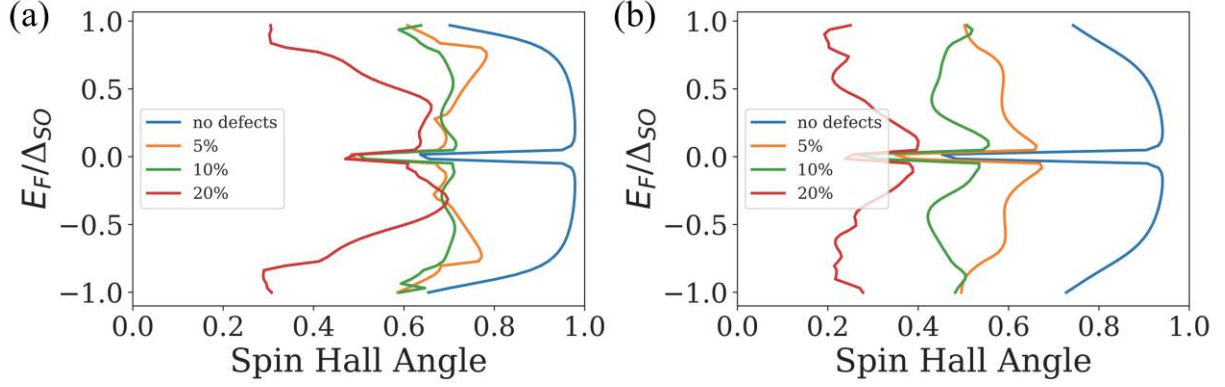


FIG. 5. Effect of edge roughness on spin-charge conversion: The spin Hall angle as a function of the normalized Fermi energy E_F for a monolayer crossbar channel with (a) a horizontal zigzag edge ribbon width of $m=20$ and a vertical armchair ribbon width of $n = 20$, and (b) a horizontal zigzag edge ribbon width of $m=10$ and a vertical armchair ribbon width of $n = 14$. The results are simulated in the linear transport regime with perfect edges and defective edges in the presence of 5%, 10%, and 20% edge roughness, respectively. The Fermi energy E_F is with reference to the middle of the bandgap and is normalized to the SOC parameter Δ_{SO} . The modeled device structure is shown in Fig. 1.

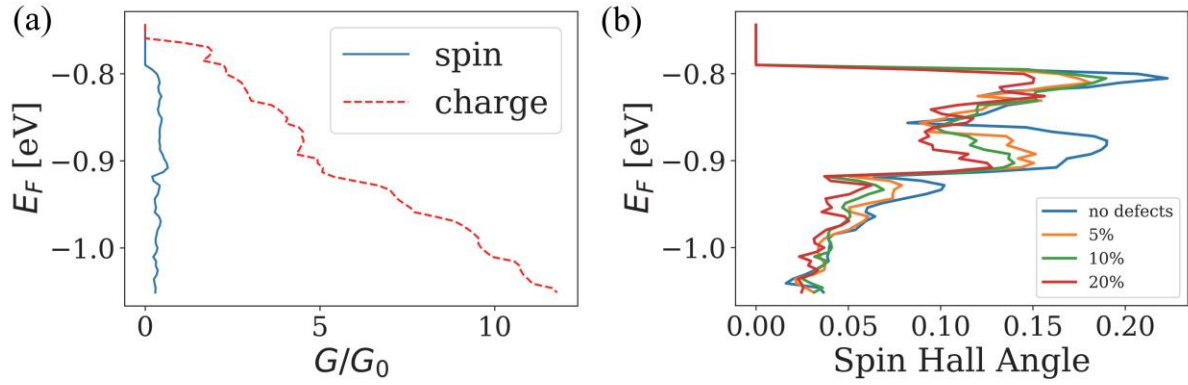


FIG. 6. (a) Charge conductance and spin conductance vs. the Fermi energy E_F with perfect edges. (b) The spin Hall angle vs. E_F for various edge roughness percentages with monolayer MoS₂ as the channel material. The horizontal ribbon has zigzag edges with a width index of $m = 25$, and the vertical part has armchair edges with a width index of $n = 20$. The results are simulated in the linear transport regime with perfect edges and defective edges in the presence of 5%, 10%, and 20% edge roughness. The modeled device structure is shown in Fig. 1.